energies

MDPI

Article

Short-Term Frequency Response of a DFIG-Based Wind Turbine Generator for Rapid Frequency Stabilization

Dejian Yang [1], Moses Kang [1], Eduard Muljadi [2], Wenzhong Gao [3], Junhee Hong [4], Jaeseok Choi [5] and Yong Cheol Kang [4,*]

1 Department of Electrical Engineering and Wind Energy Grid-Adaptive Technology (WeGAT) Research Centre, Chonbuk National University, Chonju 54896, Korea; dejian@jbnu.ac.kr (D.Y.); bass0806@jbnu.ac.kr (M.K.)
2 National Renewable Energy Laboratory, Golden, CO 80401, USA; eduard.muljadi@nrel.gov
3 Department of Electrical and Computer Engineering, University of Denver, Denver, CO 80208, USA; wenzhong.gao@du.edu
4 Department of Energy IT, Gachon University, Seoul 13120, Korea; hongpa@gachon.ac.kr
5 Department of Electrical Engineering, Gyeongsang National University, Jinju 52828, Korea; jschoi@gnu.ac.kr
* Correspondence: augustinekang33@gmail.com; Tel.: +82-10-3083-8680

Received: 12 October 2017; Accepted: 11 November 2017; Published: 14 November 2017

Abstract: This paper proposes a short-term frequency-response scheme of a doubly-fed induction generator (DFIG)-based wind turbine generator (WTG) for improving rotor speed recovery and frequency nadir. In the energy-releasing period, to improve the frequency nadir and rotor speed convergence by releasing a large amount of kinetic energy stored in the rotating masses in a DFIG-based WTG, the power reference is increased up to the torque limit referred to the power and reduces along with it for a predefined period which is determined based on the occurrence time of the frequency nadir in a power grid. Then, the reference decreases so that the rotor speed is forced to be converged to the preset value in the stable operating region of the rotor speed. In the energy-absorbing period, to quickly recover the rotor speed, the reference smoothly decreases with the rotor speed and time during a predefined period until it intersects with the maximum power point tracking curve. The simulation results demonstrate that the proposed scheme successfully achieves rapid frequency stabilization with the improved frequency nadir under various wind conditions based on the IEEE 14-bus system.

Keywords: short-term frequency response; frequency nadir; doubly-fed induction generator; torque limit; frequency stabilization; rotor speed convergence

1. Introduction

The system frequency of an electric grid should be kept within an allowable range at all times to ensure stable operation. To achieve this goal, if a large frequency event such as a generator tripping occurs, the decreased frequency should be promptly recovered to the nominal value. In a conventional electric power grid, synchronous generators that have spinning reserve increase their mechanical power by relying on the frequency deviation [1]. The frequency nadir is an important metric in maintaining the frequency stability.

For an electric power grid that has a high level of wind power penetration, variable-speed wind turbine generators (WTGs)—e.g., doubly-fed induction generator (DFIG)-based WTGs and full converter-based WTGs—perform a maximum power point tracking (MPPT) operation that extracts the maximum energy from the wind at different wind speeds [2,3]. However, this operation adversely

impacts frequency stability [4,5]. Therefore, some countries specify requirements on the frequency response of WTGs [6,7], and a number of studies on the frequency response of WTGs have been reported in the literature [8–16].

The frequency-supporting capabilities of a WTG can be classified into two groups: short-term frequency response (STFR) [8–14] and long-term frequency response [15,16]. The former temporarily releases the kinetic energy stored in the rotating masses in a WTG without the reserve power. In contrast, the latter releases the reserve power to compensate for part of the deficient power. Thus, the latter provides more contribution to frequency response; however, the latter requires the deloaded operation of a WTG, and this inevitably causes a significant loss of annual energy. Thus, this paper focuses on the STFR of a WTG and assumes that a WTG operates in an MPPT mode prior to a disturbance.

STFR schemes have been reported that release kinetic energy depending on the system frequency [8,9]; however, these schemes provide a slow response. To provide a faster response, STFR schemes were suggested that promptly increase the output power when an event is detected [10–14]. The power reference, which is defined as a function of time, increases the output, and this value is maintained for a preset period. Then, to recover the rotor speed, the power reference in [10,11] is abruptly reduced to a preset value and the reference for MPPT operation, respectively. The scheme in [11] can recover the rotor speed faster than the scheme in [10], but it causes a large second frequency drop (SFD). In addition, to ensure the stable operation of a WTG, the schemes in [10,11] should increase the power reference by a small value only. On the contrary, the schemes in [12–14] can release more kinetic energy while preventing over-deceleration because the power reference is defined as a function of the rotor speed. When an event is detected, the schemes in [12,13] simply add a constant to the reference for MPPT. In contrast, the scheme in [14] increases the reference to the torque limit referred to power, thereby improving the frequency nadir higher than those in [12,13]; then, the reference is linearly reduced with the rotor speed. To recover the rotor speed, the schemes in [12–14] reduce the reference by a small value after the rotor speed is converged to a value in the stable region; then, the reference is maintained until the reference reaches the reference for MPPT. Thus, the schemes in [12–14] can ensure a small SFD; however, the slow rotor speed is inevitable for a higher rotor speed, thereby delaying the frequency stabilization.

This paper proposes an STFR scheme of a DFIG-based WTG that ensures fast frequency stabilization while improving the frequency nadir. To achieve these objectives, the power reference function is defined in four stages. Stage I and Stage II belong to the energy-releasing period, while Stage III and Stage IV are in the energy-absorbing period. In the energy-releasing period, to speed up the rotor speed convergence while improving the frequency nadir, at Stage I, the power reference is increased up to the torque limit referred to power and reduced along with the torque limit referred to power for a predefined period. At Stage II, to converge the rotor speed into the stable operating region, the power reference decreases linearly with the rotor speed. In the energy-absorbing period, to promptly recover the rotor speed, at Stage III, the power reference smoothly decreases with the rotor speed and time during a predefined period so that it meets the reference for MPPT. At Stage IV, the rotor speed is eventually recovered to the value prior to an event along with the MPPT curve. The efficacy of the proposed scheme is verified with various wind conditions based on the IEEE 14-bus system using an electromagnetic transient program restructured version (EMTP-RV) simulator, which is a technically advanced simulation and analysis software for power system transients.

2. Modeling and Control of a DFIG-Based WTG

Figure 1a depicts a typical configuration of a DFIG-based WTG model: a wind turbine model, an induction machine, and a control system.

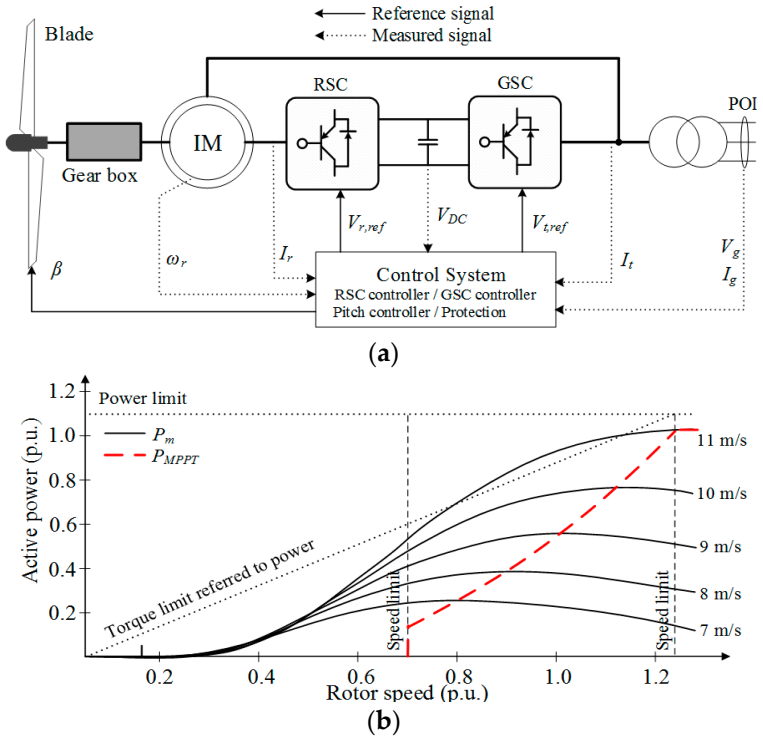

Figure 1. Typical configuration and operational characteristics of a doubly-fed induction generator (DFIG)-based wind turbine generator (WTG). (**a**) Typical configuration of a DFIG-based WTG model; (**b**) Power characteristics of a DFIG-based WTG model. I_r, I_t: current at rotor circuit and grid-side convertor (GSC) terminal; ω_r: rotor speed; $V_{r,ref}$, $V_{t,ref}$: reference rotor-side convertor (RSC) and GSC voltages; V_{DC}: DC-link voltage; V_g, I_g: voltage and current at the point of interconnection (POI).

As in [17], the mechanical power extracted from the wind, P_m, is given by:

$$P_m = \frac{1}{2}\rho A v_{wind}^3 c_P(\lambda, \beta) \quad (1)$$

where ρ is the air density in kg/m^3, A is the rotor-swept area of a DFIG-based WTG in m^2, v_{wind} is the wind speed in m/s, and c_P is the power coefficient, which is a function of tip-speed ratio, λ and pitch angle, β.

The references for a rotor-side convertor (RSC) and grid-side convertor (GSC) are determined by a DFIG-based WTG control system. The RSC controls the active and reactive powers supplied into an electric power grid; whereas the GSC maintains the DC-link voltage [18,19].

As in [20], to extract the maximum energy from the wind, the reference for MPPT operation, P_{MPPT}, is set to:

$$P_{MPPT} = 0.512 \times {\omega_r}^3 \quad (2)$$

Table 1 shows the parameters of a DFIG-based WTG used in this study. Figure 1b illustrates P_{MPPT} and the mechanical power curves at different wind speeds as indicated by a red dashed line and the black solid lines, respectively. To obtain realistic results, this paper considers the power limit and torque limit referred to power as represented by the two black dotted lines. In this paper, the maximum power and torque limits of the DFIG-based WTG are set to 1.10 p.u. and 1.07 p.u., respectively; the rate limit is set to 0.45 p.u./s [21]. The operating range of the rotor speed is from 0.70 p.u. ($\omega_{\min}$) to 1.25 p.u. ($\omega_{\max}$). In addition, when the rotor speed reaches 1.25 p.u., the pitch controller is activated.

Table 1. DFIG-based WTG parameters.

Parameters	Values	Units
Nominal apparent power	5.5	MVA
Nominal active power	5	MW
Nominal stator voltage	2.3	kV
Stator resistance	0.023	p.u.
Stator leakage reactance	0.18	p.u.
Magnetizing reactance	2.9	p.u.
Rotor resistance	0.016	p.u.
Rotor leakage reactance	0.16	p.u.
Operating range of the rotor speed	0.70–1.25	p.u.
Cut-in, rated, and cut-out wind speeds	4, 11, and 25	m/s

3. STFR Schemes of a DFIG-Based WTG

In this section, the overall operational features of the two conventional schemes in [10,14], which are represented as Scheme #1 and Scheme #2, respectively, in this paper, are briefly described. Then, the operational characteristics of the proposed scheme are described.

3.1. Scheme #1

Figure 2a illustrates the control scheme of Scheme #1 [10]. At the instant of a frequency event, Scheme #1 switches the power reference, P_{ref}, from P_{MPPT} to P_{STFR}, which is defined in the time domain. At t_0, P_{ref} instantly increases from P_0 to $P_0 + \Delta P$. At $t_0 + t_{dec}$, P_{ref} abruptly decreases from $P_0 + \Delta P$ to $P_0 - 0.5\Delta P$. At $t_0 + t_{dec} + t_{acc}$, P_{ref} is returned to P_{MPPT}. P_{ref} at Point D should be smaller than P_m so that ω_r starts recovering (see Figure 2c). To prevent over-deceleration, a small ΔP should be determined and it was set to 0.1 p.u.; t_{dec} and t_{acc} are set to 10.0 s and 20.0 s, respectively [10]. At $t_0 + t_{dec}$, to restore the ω_r, 0.15 p.u. is abruptly reduced.

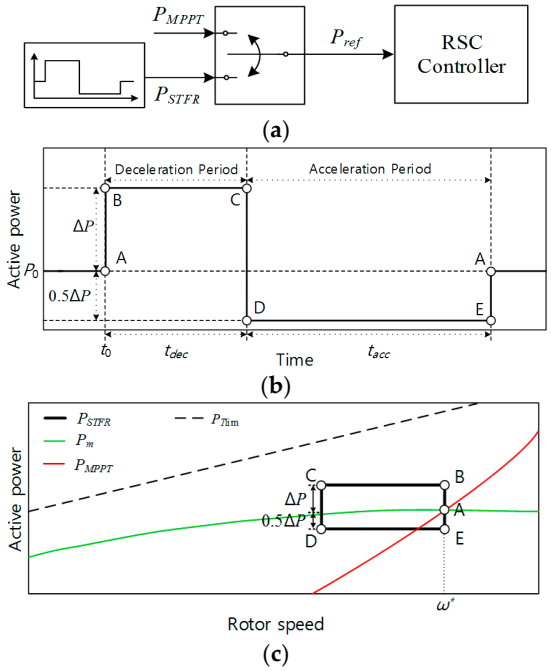

Figure 2. Operational characteristics of Scheme #1 [10]. (**a**) Control scheme of Scheme #1; (**b**) P_{STFR} of Scheme #1; (**c**) $P_{ref} - \omega_r$ trajectory of Scheme #1. P_0: power reference prior to an event; P_{STFR}: power reference during short-term frequency response (STFR); $P_{T\lim}$: torque limit referred to power; P_m: mechanical input power curve; ΔP: incremental power for STFR; t_0: instant of an event; t_{dec}, t_{acc}: deceleration and acceleration periods; ω^*: optimal rotor speed prior to an event.

3.2. Scheme #2

In Scheme #2 [14], to improve the frequency nadir while ensuring stable operation, P_{ref} is defined as a function of ω_r, as shown in Figure 3. Upon detecting an event, Scheme #2 increases P_{ref} from P_0 to $P_{Tlim}(\omega^*)$, which is the torque limit referred to power at ω^*. Thus, Scheme #2 is capable of improving the frequency nadir than that in Scheme #1 by releasing more kinetic energy.

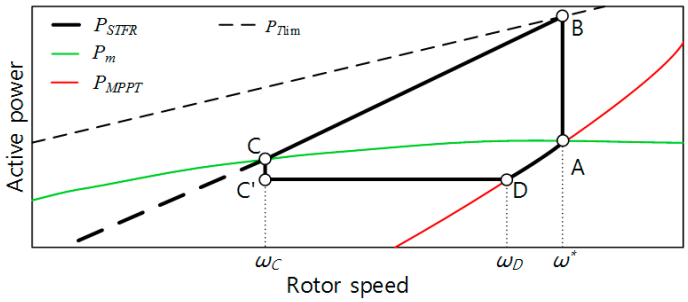

Figure 3. P_{STFR} for Scheme #2 [14]. P_{STFR}: power reference of Scheme #2; ω_C, ω_D: rotor speeds at Point C and Point D.

Then, to converge ω_r to a point in the stable region, P_{ref} is reduced as a function of ω_r (from Point B to Point C in Figure 3) as in

$$P_{ref} = \frac{P_{Tlim}(\omega*) - P_{MPPT}(\omega_{\min})}{\omega* - \omega_{\min}}(\omega_r - \omega_{\min}) + P_{MPPT}(\omega_{\min}) \quad (3)$$

where $P_{MPPT}(\omega_{\min})$ is P_{MPPT} at $\omega_{\min}$.

During this period, ω_r keeps decreasing until it converges to ω_C, which is a point of intersection of (3) and P_m. Note that ω_C is determined between $\omega_{\min}$ and ω^*; this means that ω_C is located in the stable region, and thus Scheme #2 ensures stable operation while supporting the frequency.

To recover ω_r to ω^*, Scheme #2 abruptly reduces P_{ref} at Point C, as Scheme #1 does; however, the reduced power is 0.03 p.u., which is 20% of the reduced power (0.15 p.u.) in Scheme #1. Thus, Scheme #2 causes a significantly smaller SFD than Scheme #1. At ω_C, P_{ref} is reduced to $P_{ref}(\omega_C)$ − 0.03 p.u., which is maintained until P_{ref} meets P_{MPPT} at Point D; thereafter, ω_r is returned to ω^* along with the P_{MPPT} curve. Therefore, Scheme #2 can improve the frequency nadir at a higher level while ensuring a smaller SFD than Scheme #1. However, for a higher ω^*, the ω_r recovery becomes significantly slower than that in Scheme #1, thereby delaying the frequency stabilization.

3.3. Proposed STFR Scheme of a DFIG-Based WTG for the Rapid Rotor Speed Recovery

This paper aims to improve the ω_r recovery faster than Scheme #2 while improving the frequency nadir at a higher level, thereby providing rapid frequency stabilization. As shown in Figure 4a, upon detecting an event, the proposed scheme instantly increases P_{ref} to $P_{Tlim}(\omega^*)$ as Scheme #2 does; then, P_{ref} in the proposed scheme consists of four stages. Stage I and Stage II, in which ω_r keeps decreasing until it converges to ω_C, correspond to the section from Point B to Point C in Scheme #2. Stage III corresponds to the section from Point C to Point D in Scheme #2; finally, Stage IV is the same as the section from Point D to Point A in Scheme #2. During Stage III and Stage IV, ω_r keeps increasing until ω_r reaches ω^*.

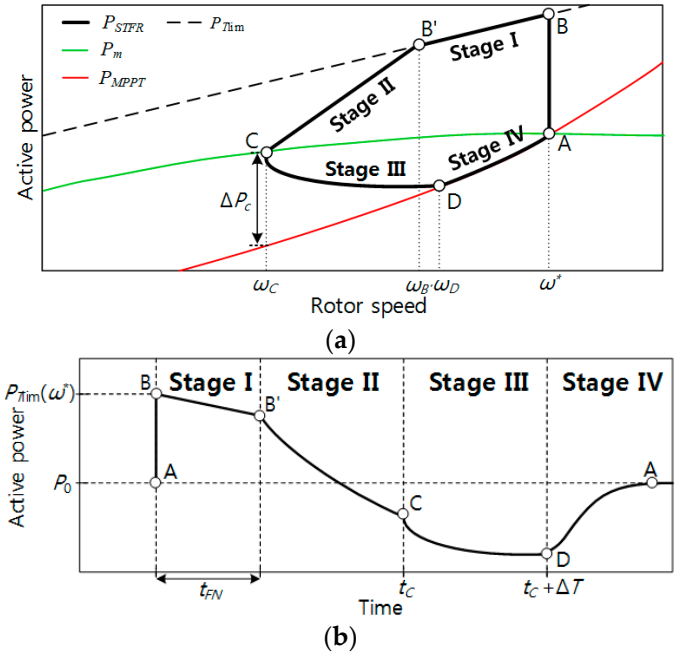

Figure 4. Operational characteristics of the proposed scheme. (**a**) Power-rotor speed trajectory of the proposed scheme; (**b**) P_{STFR} of the proposed scheme. $P_{Tlim}(\omega^*)$: torque limit referred to power at ω^*; P_{STFR}: power reference of the proposed scheme; t_C: beginning instant of Stage III; t_{FN}: period for Stage I; $\omega_{B'}$: rotor speed at Point B'.

3.3.1. Energy-Releasing Period: Stage I and Stage II

To support the frequency, the proposed scheme instantly increases P_{ref} up to $P_{Tlim}(\omega^*)$ upon detecting an event as in Scheme #2. As a result, ω_r decreases. To accelerate the ω_r convergence faster than Scheme #2, P_{ref} should be larger than that in Scheme #2 because the reduction rate of ω_r depends on the difference between P_{ref} and P_m. To do this, P_{ref} is reduced along with $P_{Tlim}(\omega_r)$ for the preset time, which is represented as t_{FN} in this paper, as in:

$$P_{ref} = P_{Tlim}(\omega_r) \quad for\, \omega_{B\prime} \leq \omega_r < \omega* \tag{4}$$

In this paper, t_{FN} is determined in association with the time of occurrence of the frequency nadir in an electric power grid. P_{ref} in (4) can not only accelerate the reduction in ω_r, but improve the frequency nadir at a higher level than the conventional schemes because the maximum kinetic energy can be released until around the frequency nadir. However, if a WTG has a smaller kinetic energy level under low wind conditions, where $P_{Tlim}(\omega^*)$ becomes larger than that under high wind conditions (see Figure 1b), a large t_{FN} can cause over-deceleration. To prevent this, in the proposed scheme, t_{FN} is set to zero if ω^* is equal to or smaller than 0.9 p.u.

At Stage II, P_{ref} is defined as

$$P_{ref} = \frac{P_{Tlim}(\omega_{B\prime}) - P_m(\omega_C)}{\omega_{B\prime} - \omega_C}(\omega_r - \omega_C) + P_m(\omega_C) \quad for\, \omega_C \leq \omega_r < \omega_{B\prime} \tag{5}$$

P_{ref} in (5) is a straight line, like it is in (3) in Scheme #2. Note that ω_C in the proposed scheme can be set to any point in the stable operating region depending on design purposes, while ω_C in Scheme #2 is fixed for a ω^*. If ω_C can be set to a value close to $\omega_{B'}$, a slope between Point B' and Point C becomes very large, thereby causing an SFD. Thus, careful attention should be paid on selecting ω_C so that it can avoid an SFD between Point B' and Point C. For comparison, ω_C in the proposed scheme is set to be the same as that in Scheme #2; this means that in Scheme #2 and the proposed scheme the

total released kinetic energy while performing STFR is the same. However, ω_r in the proposed scheme converges to ω_C faster than that in Scheme #2 because P_{ref} at Stage I and Stage II in the proposed scheme are larger. As a result, the proposed scheme can start recovering ω_r earlier than it does in Scheme #2. This helps to rapidly restore ω_r to ω^*.

It is decided that ω_r converges to ω_C if (6) is satisfied.

$$|\omega_r - \omega_C| < 0.01 \text{ p.u.} \tag{6}$$

3.3.2. Energy-Absorbing Period: Stage III and Stage IV

To recover ω_r to ω^*, Scheme #1 and Scheme #2 abruptly reduce P_{ref} by 0.15 p.u., and 0.03 p.u., respectively. Thus, Scheme #2 ensures a small SFD, but slows the ω_r recovery.

To improve the ω_r recovery to ω^* faster than Scheme #2, the power reduction at ω_C larger than 0.03 p.u. is required. However, the instant power reduction of larger than 0.03 p.u. can cause a larger SFD. To avoid this, the proposed scheme reduces the power smoothly during the preset period of ΔT instead of reducing it instantly.

In this paper, P_{ref} at Stage III is defined as:

$$P_{ref} = P_{MPPT} + \Delta P_C[-\frac{1}{\Delta T}(t - t_C) + 1] \;\; for\, \omega_C < \omega_r \leq \omega_D \tag{7}$$

where ΔP_C is $P_{ref}(\omega_C) - P_{MPPT}(\omega_C)$, as shown in Figure 4a; and ΔT is the period of Stage III.

P_{MPPT}, which is the first term in (7), is proportional to the cube of ω_r (see (2)) while the second term of (7) is a function of time. Thus, P_{ref} in (7) smoothly decreases with ω_r and t. As time goes on, ω_r increases so that P_{MPPT} increases; in addition, the second term decreases from ΔP_C to zero at $t_C + \Delta T$ (Point D), where P_{ref} reaches P_{MPPT}. Note that in the proposed scheme the duration for ω_r recovery can be controlled by setting ΔT. The use of a small ΔT leads Point D in Figure 4a to move to the left, therefore increasing the difference between P_m at Point C and P_{ref} at Point D. Thus, a small ΔT is desirable for the rapid ω_r recovery but can cause a significant SFD; in contrast, the use of a large ΔT conversely results in the small SFD but slows the ω_r recovery. In this paper, ΔT is set to 15.0 s by compromising the ω_r recovery duration and size of an SFD.

At Point D, where Stage IV starts, ω_r moves to ω^* along with P_{MPPT}.

4. Model System

Figure 5 shows the IEEE 14-bus system used to investigate the performance of the proposed scheme. It was simulated using an EMTP-RV simulator. The model system consists of five synchronous generators, static loads, and one aggregated DFIG-based wind power plant (WPP). Table 2 shows the parameters of the synchronous generators in the IEEE 14-bus system [22]. In this paper, all are modeled as steam turbine generators to simulate a power system that has a low ramping capability such as Korea's electric power grid. The steam turbine governor model of synchronous generators is the IEEEG1 [23]; the droop gains of synchronous generators are set to 5%, which is the typical setting for the synchronous generators used in Korea's electric power grid. In addition, automatic generation control is not implemented in this paper and thus the system frequency is not returned to the nominal value after the frequency is rebounded. The total load is set to approximately 540 MW and 57.4 MVAr.

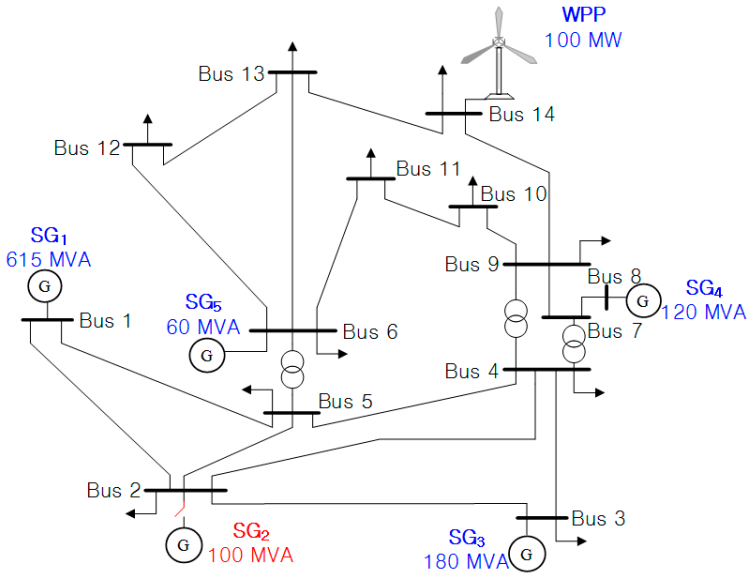

Figure 5. IEEE 14-bus system.

Table 2. Parameters of synchronous generators.

Number of Synchronous Generators	1	2	3	4	5
Rated power (MW)	615	100	180	120	60
Bus number	1	2	3	8	6
Inertia constant (s)	7	5	6	5	4

5. Case Studies

The performance of the STFR schemes of a WTG is affected by the wind speed. Thus, this section investigates the performance of STFR schemes under various wind speeds with the wind power penetration level of 18.6%; this paper defines the wind power penetration level as the installed capacity of a WPP divided by the total load [24].

Table 3 shows the initial outputs of synchronous generators and the WPP for three cases. As a disturbance, Synchronous Generator 2 (SG_2) generating approximately 100 MW is tripped out at 50.0 s for all cases.

Table 3. Initial output of synchronous generators and a wind power plant (WPP) for all cases.

Case	Load (MW)	SG_1 (MW)	SG_2 (MW)	SG_3 (MW)	SG_4 (MW)	SG_5 (MW)	WPP (MW)
1	538	180	100	90	60	38	73
2	538	202	100	90	60	38	53
3	538	218	100	90	60	38	37

The performance of the proposed STFR scheme is compared to Scheme #1 in [10] and Scheme #2 in [14]; in addition, it is compared to MPPT operation. As suggested in [10], t_{dec} and t_{acc} in Scheme #1 are set to 10.0 s and 20.0 s, respectively; ΔP is set to be 0.1 p.u. The following subsections describe the comparison results of the STFR schemes for three cases.

5.1. Effects of Wind Speeds

The wind speed affects the performance of the STFR schemes of a WTG, thereby resulting in different levels of kinetic energy in a WTG. Thus, this subsection validates the effects of high (10.0 m/s), medium (9.0 m/s), and low (8.0 m/s) speeds on the performance of the STFR schemes.

5.1.1. Case 1: Wind Speed of 10.0 m/s and Wind Power Penetration Level of 18.6%

Figure 6 illustrates the results for Case 1. In this case, t_{FN} is set to 3.0 s because the frequency nadir in the IEEE 14-bus system regularly appears approximately 3.0 s after an event. In addition, ω_C is set to 0.98 p.u.

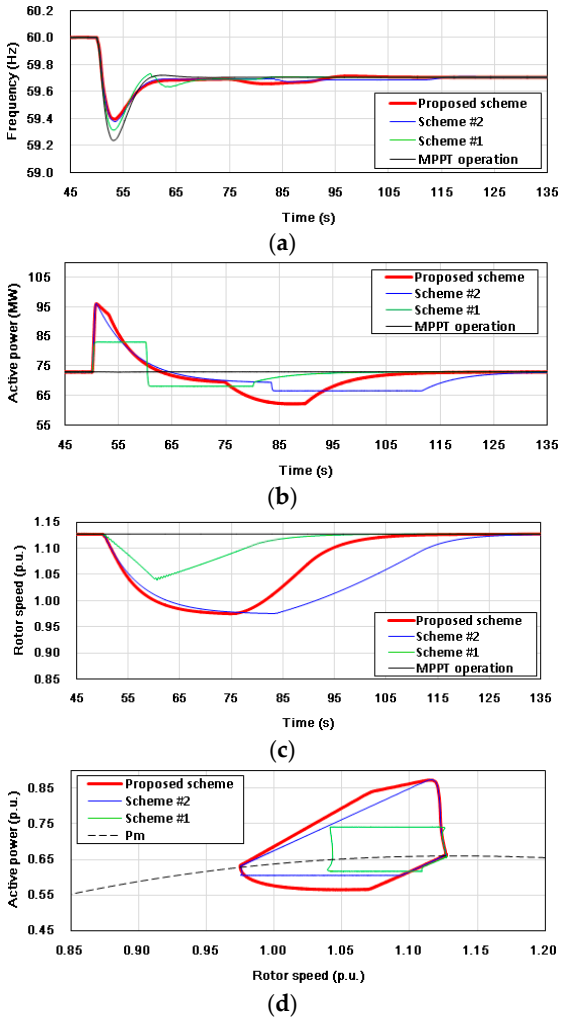

Figure 6. Results for Case 1. (**a**) system frequencies; (**b**) WPP outputs; (**c**) Rotor speeds; (**d**) Power-speed trajectories.

The frequency nadir in the proposed scheme is 59.40 Hz, which is higher than that in Scheme #2 by 0.02 Hz, and higher than that in Scheme #1 by 0.09 Hz (see Figure 6a). The frequency nadir for the proposed scheme is higher than those in the conventional schemes because the proposed scheme releases more kinetic energy until around the frequency nadir.

As shown in Figure 6c, ω_r in the proposed scheme and Scheme #2 converge to the same value of 0.98 p.u. at 75.1 s and 83.5 s, respectively. Note that ω_r in the proposed scheme is converged faster than that in Scheme #2 by 8.4 s because of a larger P_{ref} in Stage I and Stage II (energy-releasing period) even though both schemes release the same kinetic energy.

For recovering ω_r, 0.15 p.u. is instantly reduced from P_{ref} in Scheme #1 at 60.0 s, where a significant SFD of 0.098 Hz occurs. (In this study, the size of an SFD is defined as the difference between the frequency prior to an SFD and the second frequency nadir.) In Scheme #2, 0.03 p.u. is instantly reduced from P_{ref} after ω_r converges at 83.5 s, where a small SFD of 0.021 Hz occurs; however, this results in the slow ω_r recovery, therefore delaying the frequency stabilization. In contrast to the conventional

schemes, in the proposed scheme, 0.08 p.u. is smoothly reduced from P_{ref} for 15.0 s after ω_r converges at 75.1 s. The size of an SFD in the proposed scheme is 0.034 Hz, which is significantly smaller than that in Scheme #1 and slightly larger than in Scheme #2. As shown in Figure 6c, the duration for ω_r recovery is 64.5 s, which is faster than it is in Scheme #2 by 18.0 s because of the faster ω_r convergence and a larger difference between P_m and P_{ref} in Stage III. Consequently, the system frequency in the proposed scheme is stabilized significantly faster than it is in Scheme #2 with a slightly larger SFD (see Figure 6a).

As shown in Figure 6d, the proposed scheme increases P_{ref} up to the torque limit referred to power upon detecting an event and decreases P_{ref} along with $P_{T\lim}$ for 3.0 s. Afterward, P_{ref} linearly reduces to ω_C. After the reduction in P_{ref}, ω_r successfully returns to ω^*.

5.1.2. Case 2: Wind Speed of 9.0 m/s and Wind Power Penetration Level of 18.6%

Figure 7 illustrates the results for Case 2. In this case, t_{FN} is set to 3.0 s and ω_C is set to 0.86 p.u.

The frequency nadir in the proposed scheme is 59.46 Hz, which is higher than that in Scheme #2 by 0.04 Hz, and higher than that in Scheme #1 by 0.15 Hz. This is because the proposed scheme releases a larger kinetic energy than Scheme #1 and Scheme #2 until around the frequency nadir as in Case 1.

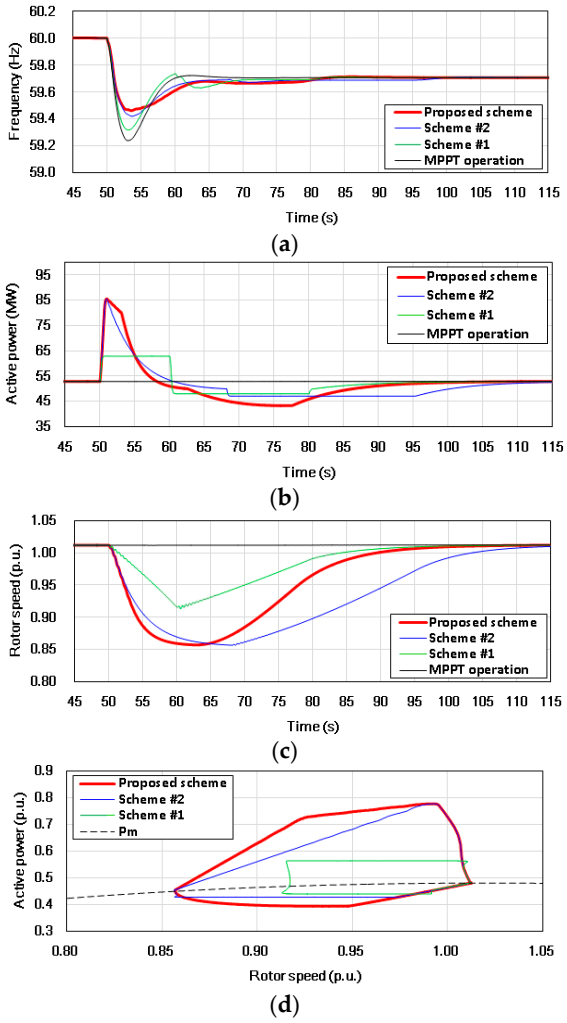

Figure 7. Results for Case 2. (**a**) system frequencies; (**b**) WPP outputs; (**c**) Rotor speeds; (**d**) Power–speed trajectories.

As in Case 1, ω_r in the proposed scheme converges to 0.86 p.u. at 63.0 s, which is faster than that in Scheme #2 by 5.3 s because of a larger P_{ref} in the energy-releasing period. To recover ω_r, Scheme #1 causes a large SFD of 0.101 Hz while Scheme #2 reduces the size of an SFD to 0.020 Hz but slow the ω_r recovery. In contrast, the proposed scheme causes a small SFD of 0.016 Hz, which is slightly smaller than in Scheme #2. Further, ω_r in the proposed scheme is recovered at 101.4 s, which is faster than that in Scheme #2 by 16.4 s (see Figure 7c) because of the faster ω_r convergence in Stage I and Stage II and a larger difference between P_m and P_{ref} in Stage III. Thus, the system frequency is stabilized faster than it is in Scheme #2. Thus, the proposed scheme is capable of ensuring the rapid frequency stabilization while improving the frequency nadir.

5.1.3. Case 3: Wind Speed of 8.0 m/s and Wind Power Penetration Level of 18.6%

Figure 8 illustrates the results for Case 3 with the lower wind speed than that in the previous cases; thus, the smaller kinetic energy is stored. In this case, t_{FN} is set to zero because ω_r prior to an event is 0.9 p.u.; thus, P_{ref} in Stage I and Stage II are the same in Scheme #2 and the proposed scheme. As a result, the frequency nadir and t_C in the proposed scheme and Scheme #2 are the same. The frequency nadir in Scheme #2 and the proposed scheme is 59.41 Hz, which is higher than it is in Scheme #1 by 0.10 Hz (see Figure 8a). In addition, similar to the previous cases, Scheme #1 causes a large SFD while Scheme #2 does a small SFD with the slow ω_r recovery. In contrast, the proposed scheme ensures the rapid ω_r recovery with a small SFD which is slightly larger than that in Scheme #2. As a result, the proposed scheme is able to ensure the rapid frequency stabilization.

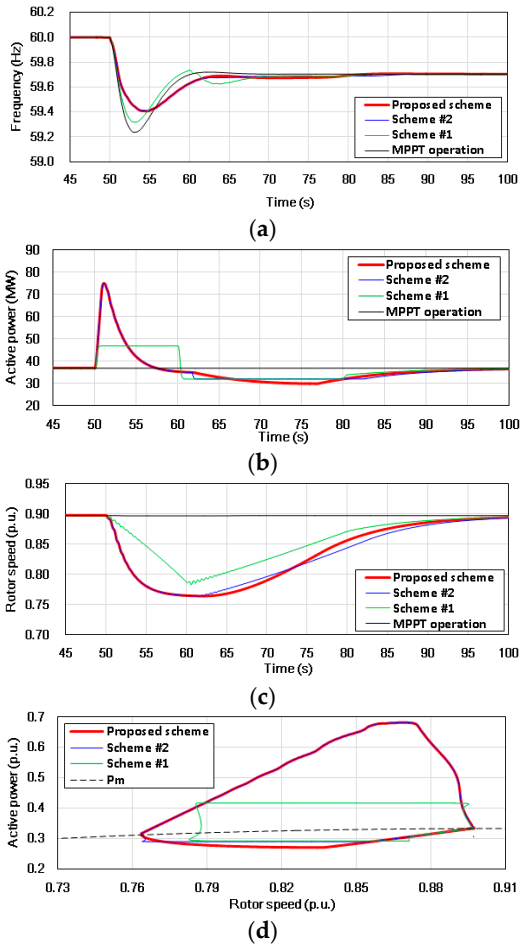

Figure 8. Results for Case 3. (**a**) system frequencies; (**b**) WPP outputs; (**c**) Rotor speeds; (**d**) Power-speed trajectories.

The results of the previous three cases clearly indicate that the proposed scheme is able to improve the frequency nadir by releasing the maximum power for the predefined period and ensures the faster ω_r recovery and frequency stabilization under various wind conditions.

Table 4 shows a comparison of the numerical results for three cases in terms of the released kinetic energy for 3.0 s, frequency nadir, time to rotor speed recovery after an event, and size of an SFD. Because the released kinetic energy for 3.0 s in the proposed scheme is larger than those in the conventional schemes, the frequency nadir is higher than it is in the conventional schemes in all cases except for Case 3; this is because in the low wind speed there is no Stage I in the proposed scheme. The rotor speed recovery is faster than in Scheme #2 because of the faster ω_r convergence and larger difference between P_m and P_e at Stage III. In addition, the proposed scheme causes an SFD, which is much smaller than that of Scheme #1 and slightly larger than or similar to that Scheme #2 since the proposed scheme smoothly decreases P_{ref} during Stage III. Thus, the proposed scheme is capable of ensuring the rapid frequency stabilization.

Table 4. Comparisons results for all cases.

Indices for Evaluaing STFR Schemes	Control Schemes	Case 1	Case 2	Case 3
Released kinetic energy for 3.0 s (s)	Proposed scheme	0.60	0.80	0.77
	Scheme #2	0.55	0.71	0.77
	Scheme #1	0.28	0.28	0.28
Frequency nadir (Hz)	Proposed scheme	59.40	59.46	59.41
	Scheme #2	59.38	59.42	59.41
	Scheme #1	59.31	59.31	59.31
	MPPT operation	59.24	59.24	59.24
Time for the rotor speed recovery (s)	Proposed scheme	64.5	51.4	50.4
	Scheme #2	82.5	67.8	55.2
	Scheme #1	49.7	49.7	49.7
Size of an SFD (Hz)	Proposed scheme	0.034	0.016	0.014
	Scheme #2	0.021	0.020	0.003
	Scheme #1	0.098	0.101	0.100

6. Conclusions

This paper proposes an STFR scheme of a DFIG-based WTG for ensuring the rapid frequency stabilization while improving the frequency nadir. In the energy-releasing period, the proposed scheme increases the power reference up to the torque limit referred to power and reduces along with the torque limit referred to power for a predefined period, and then the reference decreases so that the rotor speed converges to the preset value. In the energy-absorbing period, the reference is smoothly reduced with the rotor speed and time during a predefined period so that it meets the reference for MPPT.

The simulation results clearly demonstrate that the proposed scheme improves the frequency nadir under various wind conditions. Further, the proposed scheme ensures the faster rotor speed recovery than Scheme #2 with a slightly larger SFD than Scheme #2, thereby improving the frequency stabilization.

The advantages of the proposed scheme are that it can ensure the rapid frequency stabilization while improving the frequency nadir under various wind conditions. Therefore, the proposed scheme will provide potential solutions to ancillary services by helping stabilize the system frequency in an electric power grid.

Acknowledgments: This work was supported by the Human Resources Development of Korea Institute of Energy Technology Evaluation and Planning (KETEP) grant funded by the Ministry of Trade, Industry and Energy. (No. 20174030201440). The National Renewable Energy Laboratory's (NREL's) contribution to this work was supported by the U.S. Department of Energy under Contract no. DE-AC36-08-GO28308 with NREL. Funding provided by DOE Wind Energies Technologies Office.

Author Contributions: All the authors contributed to publish this paper. Dejian Yang, Moses Kang, and Yong Cheol Kang mainly proposed the proposed scheme. Dejian Yang, Moses Kang, and Yong Cheol Kang carried out the simulation tests; Eduard Muljadi, Wenzhong Gao, Junhee Hong, Jaesoek Choi, and Yong Cheol Kang revised the original scheme. Writing was done by Dejian Yang, Moses Kang, Eduard Muljadi, Wenzhong Gao, Junhee Hong, Jaeseok Choi, and Yong Cheol Kang. Final review was done by all the authors.

Conflicts of Interest: The authors declare no conflict of interest.

References

1. Machowski, J.; Bialek, J.W.; Bumby, J.R. *Power System Dynamics: Stability and Control*, 2nd ed.; John Wiley & Sons, Ltd.: Chichester, UK, 2008.
2. Phan, D.-C.; Yamamoto, S. Maximum energy output of a DFIG wind turbine using an improved MPPT-curve method. *Energies* **2015**, *8*, 11718–11736. [CrossRef]
3. Zhang, X.; Huang, C.; Hao, S.; Chen, F.; Zhai, J. An Improved Adaptive-Torque-Gain MPPT Control for Direct-Driven PMSG Wind Turbines Considering Wind Farm Turbulences. *Energies* **2016**, *9*, 997. [CrossRef]
4. Kim, Y.-S.; Chung, I.-Y.; Moon, S.-I. An analysis of variable-speed wind turbine power-control methods with fluctuating wind speed. *Energies* **2013**, *6*, 3323–3338. [CrossRef]
5. Shi, Q.; Wang, G.; Ma, W.; Fu, L.; Wu, Y.; Xing, P. Coordinated Virtual Inertia Control Strategy for D-PMSG Considering Frequency Regulation Ability. *J. Elect. Eng. Technol* **2016**, *11*, 1921–1935. [CrossRef]
6. Tsili, M.; Papathanassiou, S. A review of grid code technical requirements for wind farms. *IET Renew. Power Gener.* **2009**, *3*, 308–332. [CrossRef]
7. Hydro Québec. Transmission Provider Technical Requirements for the Connection of Power Plants to the Hydro Québec Transmission System. Hydro Québec, Montréal, Québec, 2009. Available online: http://www.hydroquebec.com/transenergie/fr/commerce/pdf/exigence_raccordement_fev_09_en.pdf (accessed on 12 November 2017).
8. Ekanayake, J.B.; Jenkins, N. Comparison of the response of doubly-fed and fixed-speed induction generator wind turbines to changes in network frequency. *IEEE Trans. Energy Convers.* **2004**, *19*, 800–802. [CrossRef]
9. Margaris, I.D.; Hansen, A.D.; Sørensen, P.; Hatziargyriou, N.D. Illustration of modern wind turbine ancillary services. *Energies* **2010**, *3*, 1290–1302. [CrossRef]
10. Ullah, N.R.; Thiringer, T.; Karlsson, D. Temporary primary frequency control support by variable speed wind turbines—Potential and applications. *IEEE Trans. Power Syst.* **2008**, *23*, 601–612. [CrossRef]
11. Hansen, A.D.; Altin, M.; Margaris, I.D.; Lov, F.; Tarnowski, G.C. Analysis of the short-term overproduction capability of variable speed wind turbines. *Renew. Energy* **2014**, *68*, 326–336. [CrossRef]
12. Wu, Z.; Gao, W.; Wang, X.; Kang, M.; Hwang, M.; Kang, Y.C.; Gevogian, V.; Muljadi, E. Improved inertial control for permanent magnet synchronous generator wind turbine generators. *IET Renew. Power Gener.* **2016**, *10*, 1366–1373. [CrossRef]
13. Kang, M.; Muljadi, E.; Hur, K.; Kang, Y.C. Stable adaptive inertial control of a doubly-fed induction generator. *IEEE Trans. Smart Grid* **2016**, *7*, 2971–2979. [CrossRef]
14. Kang, M.; Kim, K.; Muljadi, E.; Park, J.-W.; Kang, Y.C. Frequency control support of a doubly-fed induction generator based on the torque limit. *IEEE Trans. Power Syst.* **2016**, *31*, 4575–4583. [CrossRef]
15. Zhang, Z.-S.; Sun, Y.-Z.; Lin, J.; Li, G.-J. Coordinated frequency regulation by doubly fed induction generator-based wind power plants. *IET Renew. Power Gener.* **2012**, *6*, 38–47. [CrossRef]
16. Almeida, R.G.; Lopes, J.A.P. Participation of doubly fed induction wind generators in system frequency regulation. *IEEE Trans. Power Syst.* **2007**, *22*, 944–950. [CrossRef]
17. Lotfy, M.; Senjyu, T.; Farahat, M.; Abdel-Gawad, A.; Yona, A. A frequency control approach for hybrid power system using multi-objective optimization. *Energies* **2017**, *10*, 80. [CrossRef]
18. Hong, M.; Xin, H.; Liu, W.; Xu, Q.; Zheng, T.; Gan, D. Critical Short Circuit Ratio Analysis on DFIG Wind Farm with Vector Power Control and Synchronized Control. *J. Elect. Eng. Technol* **2016**, *11*, 320–328. [CrossRef]
19. Papadimitriou, C.N.; Vovos, N.A. Transient response improvement of microgrids exploiting the inertia of a doubly-fed induction generator (DFIG). *Energies* **2010**, *3*, 1049–1066. [CrossRef]
20. Shen, B.; Mwinyiwiwa, B.; Zhang, Y.; Ooi, B. Sensorless maximum power point tracking of wind by DFIG using rotor position phase lock loop. *IEEE Trans. Power Electron.* **2009**, *24*, 942–951. [CrossRef]

21. Wang, Y.; Delille, G.; Bayem, H.; Guilaud, X.; Francois, B. High wind power penetration in isolated power systems—Assessment of wind inertial and primary frequency responses. *IEEE Trans. Power Syst.* **2013**, *28*, 2412–2420. [CrossRef]
22. Sutter, J.; Muriithi, C. Analysis of power system transient stability due to increased integration of geothermal power. In Proceedings of the 39th Workshop on Geothermal Reservoir Engineering, Stanford, CA, USA, 24–26 February 2014.
23. Byerly, R.T.; Aanstad, O.; Berry, D.H.; Dunlop, R.D.; Ewart, D.N.; Fox, B.M.; Johnson, L.H.; Tschappat, D.W. Dynamic models for steam and hydro turbines in power system studies. *IEEE Trans. Power Appar. Syst.* **1973**, *92*, 1904–1915.
24. Ackermann, T. *Wind Power in Power Systems*, 2nd ed.; John Wiley & Sons, Ltd.: Chichester, UK, 2012.